Physics-informed data-driven prediction of turbulent reacting flows with Lyapunov analysis and sequential data assimilation

Luca Magri and Nguyen Anh Khoa Doan

Abstract High-fidelity simulations of turbulent reacting flows enable scientific understanding of the physics and engineering design of practical systems. Whereas direct numerical simulation (DNS) is the most suitable numerical tool to understand the physics, under-resolved and large-eddy simulations offer a good compromise between accuracy and computational effort in the prediction of engineering flows. This compromise speeds up the computations but reduces the space-and-time accuracy of the prediction. The objective of this chapter is to (i) evaluate the predictability horizon of turbulent simulations with chaos theory, and (ii) enable the space-and-time accurate prediction of rare and transient events using a Bayesian statistical learning approach based on data assimilation. The methods are applied to DNS of Moderate or Intense Low-oxygen Dilution (MILD) combustion. The predictability provides an estimate of the time horizon within which the occurrence of ignition kernels and deflagrative modes, which are considered here as rare and transient events, can be accurately predicted. The accurate detection of ignition kernels and their evolution towards deflagrative structures are well-captured on a coarse (under-resolved) grid when data is assimilated from a costly refined DNS. Physically, such an accurate prediction is important to understand the stabilization mechanism of MILD combustion. These techniques enable the space-and-time-accurate prediction of rare and transient events in turbulent flows by combining under-resolved simulations and experimental data, for example, from engine sensors. This opens up new possibilities for on-the-fly calibration of reduced-order models for turbulent reacting flows.

Luca Magri
University of Cambridge, Department of Engineering, Trumpington Street, CB2 1PZ, Cambridge, United Kingdom,
Institute for Advanced Study TU Munich, Germany (visiting fellowship)
e-mail: lm547@cam.ac.uk

Nguyen Anh Khoa Doan
Technische Universität München, FakultÃ€t fÃŒr Maschinenwesen, Boltzmannstraße 15, 85747, Garching, Germany
e-mail: doan@tfd.mw.tum.de

1 Introduction

Turbulent flows are chaotic flows. As such, the space-and-time accurate prediction of the solution is difficult to achieve because of the butterfly effect [29]: Two nearby initial conditions, which can differ by a very small amount, will practically diverge in time from each other with an exponential rate. This divergence rate is the dominant Lyapunov exponent. Whereas the statistics of turbulent flows are not significantly affected by tiny perturbations, the instantaneous solution is. (Having accurate predictions on the instantaneous solution is crucial for the prediction of rare and transient events.) For example, running the same code with the same initial conditions on a different number of processors should in principle provide two statistically equivalent solutions, but with completely different instantaneous fields after a few time steps. This fact is well-known in turbulent flows [5, 15, 37]. Albeit the butterfly effect seems to be a showstopper for the time-accurate prediction of turbulent flows, such a prediction can be greatly aided by physics-informed data-driven methods. In this chapter, first, we use dynamical systems theory to estimate the predictability of simulations with the Lyapunov time. Second, we improve the space-and-time accurate prediction of rare and transient events with statistical learning by data assimilation. The turbulent reacting flow under investigation is relevant to Moderate or Intense Low-oxygen Dilution (MILD) combustion.

Dynamical systems theory provides the predictability of a chaotic simulation, which is the time scale after which the trajectories diverge due to the butterfly effect. There exist different approaches to characterize a chaotic solution [5, 15, 38]. On one hand, geometric approaches estimate the fractal dimension of the chaotic attractor, which provides an estimate of the active degrees of freedom of the chaotic dynamical system. An accurate measure is the Hausdorff dimension [19], which is often approximated by box counting, based on phase-space partitioning and correlation dimension based on time series analysis [24]. On the other hand, dynamical approaches estimate the entropy content of the solution, for example via the Kolmogorov-Sinai entropy, and the separation rate of two nearby solutions via the Lyapunov exponents. The dominant Lyapunov exponent is a practical measure to compute the predictability of large scale simulations because it (i) is easy to calculate [5] and (ii) does not depend on the initial conditions in ergodic processes [22]. In large scale fluid-dynamics simulations, the Lyapunov exponent was calculated in channel and bluff-body flows[4], homogeneous isotropic turbulence [31, 32], reacting and non-reacting turbulent jets [32], a two-dimensional airfoil [20], backward-facing step [33], partially-premixed flames [23], to name only a few.

Once the predictability of the simulation is estimated, we assimilate data from a refinded DNS on a coarse grid by statistical learning. Statistical learning by data assimilation finds the statistically optimal combination of model predictions and observations by combining concepts from control theory, probability theory and dynamic programming. The data assimilation technique used in this study is the ensemble Kalman filter [6, 17]. In the ensemble Kalman filter, a Monte Carlo approach is used to estimate the statistics at every timestep [14], which makes it (i) a computationally efficient technique in terms of storage requirements, (ii) amenable

to parallel computing and (iii) non-intrusive. Compared to other data assimilation techniques based on the Kalman filter, e.g., the extended Kalman filter, the ensemble Kalman filter is particularly suitable for highly nonlinear systems [18], such as turbulent diffusion flames [28] and premixed flames [42, 43], the latter of which display strongly nonlinear events, such as cusp formation and pinch-off. In non-reacting flows, the ensemble Kalman filter was applied to the prediction of aerodynamic flows [9, 10]. As argued in [43], data assimilation is practically useful to *make a qualitative reduced-order model quantitatively accurate*.

MILD combustion is a concept for future low-emission and high energy efficiency combustion devices. This concept utilizes exhaust gas recirculation (EGR) to achieve a high reactant temperature and low oxygen environment, which are crucial to obtain the high energy efficiency and low pollutant emissions [8]. However, because of those particular turbulence and chemical conditions with recirculating gases carrying radicals, the physical understanding of MILD combustion is challenging. Indeed, in contrast to conventional combustion, reaction zones in MILD combustion have been shown both experimentally and from DNS to be volumetrically distributed [35], interacting with each other leading to a complex morphology [13, 30]. Furthermore, both ignition and deflagrative modes of combustion coexist, whose interaction contributes significantly to the global heat release dynamics [11]. However, despite the insight gained in these previous studies, the mechanism leading to the occurrence of the ignition kernels and the stabilization of deflagrative flames remains unknown, making their prediction a hard task. The objective of this chapter is to (i) calculate the predictability of MILD combustion case under investigation by determining its Lyapunov exponent for different grids, and (ii) make an under-resolved DNS more predictive for the space-and-time-accurate evolution of chemical reactions, in particular, the occurrence of ignition kernels and their evolution into deflagrative structures. The second goal is achieved by statistical learning with Bayesian data assimilation, in particular, with the ensemble Kalman filter.

In Section 2, the fundamentals of Lyapunov analysis from chaos theory are presented to estimate the predictability time. A practical and non-intrusive algorithm for the calculation of the (dominant) Lyapunov exponent and corresponding covariant Lyapunov vector is described. In Section 3, the ensemble Kalman filter is introduced with a Bayesian approach. The algorithm is shown step by step for parallel computing. In Section 4, the MILD combustion simulation is explained along with the DNS setup. In Section 5, the predictability and ensemble-Kalman filtered DNS are computed for MILD combustion. The chapter ends with conclusions and future directions.

2 Lyapunov analysis from chaos theory

This section introduces the key concepts and results of Oseledets' theorem [34], which lay out the fundamentals of Lyapunov analysis [21]. The turbulent reacting flow problem is governed by partial differential equations, i.e., the Navier-Stokes equations, mass and energy conservation, and equations for the chemistry. On spatial

discretization, the turbulent reacting problem can be cast as an nonlinear autonomous dynamical system

$$\begin{cases} \dot{\boldsymbol{q}}(t) = \boldsymbol{F}(\boldsymbol{q}(t), \boldsymbol{\theta}) \\ \boldsymbol{q}(0) = \boldsymbol{q}_0 \end{cases}, \tag{1}$$

where $\dot{(\,)} \equiv d(\,)/dt$; $\boldsymbol{q} \in \mathbb{R}^{N_{dof}}$ is the state vector (e.g., pressure, velocity, species, etc., at each discrete location), where N_{dof} denotes the degrees of freedom from numerical discretization of the spatial derivatives; $\boldsymbol{\theta}$ is the vector containing the parameters of the system; and $\boldsymbol{F} : \mathbb{R}^{N_{dof}} \rightarrow \mathbb{R}^{N_{dof}}$ is a nonlinear function, which encapsulates the discretized boundary conditions. The subscript 0 denotes the initial condition. In this chapter, the parameters are constant, therefore, the dependency on $\boldsymbol{\theta}$ will be dropped unless necessary for clarity. In Lyapunov analysis, we calculate the evolution of infinitesimal perturbations. The solution is split, accordingly, as

$$\boldsymbol{q}(t) = \bar{\boldsymbol{q}}(t) + \boldsymbol{q}'(t), \tag{2}$$

where $\bar{\boldsymbol{q}}(t)$ is the original (unperturbed) solution of (1), and $\boldsymbol{q}'(t)$ is the infinitesimal perturbation such that $||\boldsymbol{q}'(t)|| \sim O(\epsilon)$, where $\epsilon \rightarrow 0$. The perturbation is governed by the tangent equation

$$\begin{cases} \dot{\boldsymbol{q}}' = \boldsymbol{J}(t)\boldsymbol{q}' \\ \boldsymbol{q}'(0) = \boldsymbol{q}'_0 \end{cases}, \tag{3}$$

where $\boldsymbol{J}(t) \equiv \frac{d\boldsymbol{F}}{d\boldsymbol{q}}\big|_{\bar{\boldsymbol{q}}(t)}$ is the Jacobian. In a turbulent flow, the Jacobian is time-dependent because the unperturbed solution is chaotic. The formal evolution of the perturbation, $\boldsymbol{q}'$, is given by the tangent propagator, which maps $\boldsymbol{q}'$ from time t to time $\tilde{t}$, as

$$\boldsymbol{q}'(t + \tilde{t}) = \boldsymbol{M}(t, \tilde{t})\boldsymbol{q}'(t), \tag{4}$$

where $\dot{\boldsymbol{M}} = \boldsymbol{J}(\tilde{t})\boldsymbol{M}$ with $\boldsymbol{M}(t, 0) = \boldsymbol{I}$ and $\boldsymbol{I}$ being the identity matrix. From Eq. (3), the norm of an infinitesimal perturbation, $\boldsymbol{q}'_0$, asymptotically evolves as an exponential [34]

$$||\boldsymbol{q}'(\tilde{t})|| = ||\boldsymbol{q}'_0|| e^{\lambda(\boldsymbol{q}'_0, \bar{\boldsymbol{q}})\tilde{t}} \qquad \tilde{t} \rightarrow \infty. \tag{5}$$

The characteristic Lyapunov exponent is defined as

$$\lambda(\boldsymbol{q}'_0, \bar{\boldsymbol{q}}) = \lim_{\tilde{t}\rightarrow\infty} \frac{1}{\tilde{t}} \log \frac{||\boldsymbol{M}(0, \tilde{t})\boldsymbol{q}'_0||}{||\boldsymbol{q}'_0||} = \lim_{\tilde{t}\rightarrow\infty} \frac{1}{\tilde{t}} \log \frac{||\boldsymbol{q}'(\tilde{t})||}{||\boldsymbol{q}'_0||}. \tag{6}$$

Physically, the Lyapunov exponent is the average exponential expansion rate of an infinitesimal volume of the phase space, which moves along the attractor. A chaotic system, hence a turbulent flow, has at least one positive (unstable) Lyapunov exponent. In other words, a turbulent flow is characterized by an unstable tangent space. Furthermore, in a turbulent flow, there always exists a zero Lyapunov exponent, which is associated with the neutrally stable direction of the unperturbed solution,

$\bar{\boldsymbol{q}}(t)$. As mathematically and numerically shown by [25, 26], (i) if the attractor is a steady solution, the Lyapunov exponents are equal to the real part of the eigenvalues of the Jacobian at the fixed point; and (ii) if the attractor is a periodic solution, the Lyapunov exponents are equal to the real part of the Floquet exponents. The Lyapunov exponent is norm-independent, however, some norms are more physically significant than others. Oseledets' theorem [34] proves that there exist N Lyapunov exponents $\lambda_1 \geq \lambda_2 \geq \cdots \geq \lambda_{N_{dof}}$, which are constants of the chaotic attractor. To each Lyapunov exponent, λ_j, there exists an associated covariant Lyapunov vector, $\boldsymbol{\phi}_j$, which is the solution of

$$\frac{d\boldsymbol{\phi}_j}{d\tilde{t}} = \boldsymbol{J}\boldsymbol{\phi}_j - \lambda_j \boldsymbol{\phi}_j. \tag{7}$$

In this chapter, we do not consider degenerate Lyapunov exponents, which, however, can appear in thermoacoustic oscillations [25, 26]. Equation (7) shows that a covariant Lyapunov vector is evolved by the tangent system and has bounded norm because the second term on the right-hand side suppresses the exponential growth. A tangent vector, $\boldsymbol{q}'_0$, can be decomposed in a basis of covariant Lyapunov vectors, $\{\boldsymbol{\phi}_1, \cdots, \boldsymbol{\phi}_{N_{dof}}\}$. Assuming ergodicity [34, 38], the Lyapunov exponents are independent of the initial conditions, i.e., $\lambda(\boldsymbol{q}'_0, \bar{\boldsymbol{q}}) = \lambda_j$. Figure 1 illustrates pictorially the significance of Lyapunov exponents and covariant Lyapunov vectors. Three covariant Lyapunov vectors are shown at two different instants, each associated with a different Lyapunov exponent, which can be positive (unstable, red colour), zero (neutrally stable, orange colour) and negative (stable, green colour).

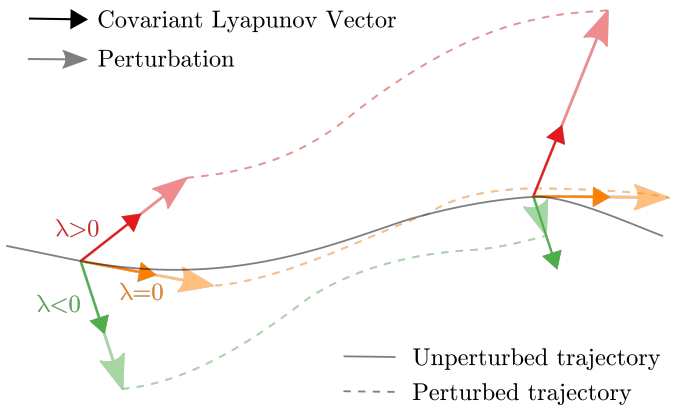

Fig. 1: Schematic of the significance of unstable (red), neutral (orange) and stable (green) covariant Lyapunov vectors and exponents [25].

2.1 Non-intrusive computation of the dominant Lyapunov exponent and covariant Lyapunov vector

We focus on the dominant Lyapunov exponent and covariant Lyapunov vector. The adjective "dominant" will be dropped for brevity unless necessary for clarity. Moreover, the dominant Lyapunov exponent will be denoted λ, i.e., the subscript 1 is dropped. Obtaining accurate estimates of the Lyapunov exponent and covariant Lyapunov vector is straightforward even in large-scale simulations. A non-intrusive method is based on the calculation of the *separation* trajectory, also known as the *error* trajectory. The separation trajectory is the difference between two nearby trajectories (which can be Eulerian fields), which originate from two close initial conditions. Because it is almost sure for the separation trajectory to have a component–even miniscule–in the direction of the dominant covariant Lyapunov vector, the separation trajectory will almost surely diverge along the covariant vector with an exponential divergence rate provided by the Lyapunov exponent. This is why the (dominant) Lyapunov exponent and (dominant) covariant Lyapunov vector are of paramount importance in chaotic flows. They can be calculated as described in the following practical and non-intrusive algorithm.

1. **Statistically converged solution.** Run a numerical simulation (1) until statistical convergence is reached ($\bar{\boldsymbol{q}}(t)$).
2. **Reset time**, $t = t_0$.
3. **Perturb**. At $t = t_0$, evaluate the perturbed solution $\boldsymbol{q}^*$ as

$$\boldsymbol{q}^*(t_0) = \bar{\boldsymbol{q}}(t_0) + \epsilon||\bar{\boldsymbol{q}}(t_0)||, \tag{8}$$

   where ϵ is a small number, typically in the range $10^{-9} - 10^{-3}$ and $||\boldsymbol{q}(t_0)||$ is a norm of order 1.
4. **Separation trajectory.** Advance both solutions, $\bar{\boldsymbol{q}}(t_0)$ and $\boldsymbol{q}^*(t_0)$, to some time t_f and evaluate the separation trajectory

$$\Delta\boldsymbol{q}(t) = \boldsymbol{q}^*(t) - \bar{\boldsymbol{q}}(t) \qquad t_0 \le t \le t_f. \tag{9}$$

5. **Identification of the linear region** $t_1 \le t \le t_2$ where $\ln(\|\Delta\boldsymbol{q}(t)\|)$ grows linearly. t_f in item 4 must be larger than t_2. If the linear region of the separation trajectory looks noisy, i.e., the local Lyapunov exponent markedly fluctuates, an ensemble simulation is recommended.
6. **Covariant Lyapunov vector.** This is the separation trajectory in the linear region, i.e., $\Delta\boldsymbol{q}(t) \quad t_1 \le t \le t_2$.
7. **Lyapunov exponent.** Because of (5), the Lyapunov exponent is the slope of the linear region, which can be obtained by linear regression

$$\lambda = \frac{1}{t_2 - t_1} \ln\left(\frac{\|\Delta\boldsymbol{q}(t_2)\|}{\|\Delta\boldsymbol{q}(t_1)\|}\right). \tag{10}$$

2.1.1 Predictability

Several definitions of predictability are offered in the literature [5]. However, for the purpose of this chapter, the *predictability* is defined as the *Lyapunov time*, which is the inverse of the Lyapunov exponent

$$t_p \equiv \frac{1}{\lambda}. \tag{11}$$

From Eq.(10), the predictability is the time that a norm of the separation trajectory takes to get amplified by $e \approx 2.718$. Physically, the predictability provides a time scale for the divergence of two nearby trajectory due to the chaotic nature of turbulent flows. Nastac et al [32] showed that the Lyapunov time scale is slightly larger than the Kolmogorov time scale for both forced homogeneous isotropic turbulence and turbulent jets. The predictability is an important factor for the time-accurate calculation of rare and transient events, such as extinction and re-ignition. Because these rare and transient events occur within a small time scale, the numerical simulation and grid should accurately resolve the dynamics within the predictability. In turbulent (reacting and non-reacting) large-eddy and direct numerical simulations, as the grid resolution approaches the smallest physical scales, the Lyapunov exponent, hence predictability, reaches a plateau [32]. Therefore, the Lyapunov exponent was proposed as a metric to assess the quality of a large-eddy simulation [32]: If grid a has the same Lyapunov exponent as grid b, the grid with fewer degrees of freedom can be used to predict rare and transient deterministic events.

3 Data assimilation from Bayesian inference

Data assimilation is a method to make a model more predictive given data from external observations. The physical model provides a prediction on the solution, which is called *forecast*, which is *updated* with a statistical learning algorithm to provide a more accurate state, which is called *analysis*. Data assimilation is here treated as a problem in Bayesian inference, where existing knowledge is quantified in the form of a probability distribution over candidate solutions. When external data becomes available, the probability distribution is updated, effectively combining the existing knowledge with the data. To introduce data assimilation as a Bayesian problem, we consider the nonlinear dynamical system (1) at discrete times denoted by the subscript k. The evolution of the state is governed by the deterministic physical model $\boldsymbol{F}$, its parameters $\boldsymbol{\theta}$ and the initial condition $\boldsymbol{q}_0$. The data assimilation problem is cast as a probabilistic state space model

$$\boldsymbol{q}_k = \boldsymbol{q}_{k-1} + \int_{t_{k-1}}^{t_k} \boldsymbol{F}(\boldsymbol{q}(t), \boldsymbol{\theta})\, \mathrm{d}t \sim p(\boldsymbol{q}_k \mid \boldsymbol{q}_{k-1}, \boldsymbol{\theta}, \boldsymbol{F}), \tag{12}$$

$$\boldsymbol{y}_k = \boldsymbol{M}(\boldsymbol{q}_k) \sim p(\boldsymbol{y}_k \mid \boldsymbol{q}_k). \tag{13}$$

The states $\boldsymbol{q}_k$ and the observations $\boldsymbol{y}_k$ are considered realizations inside their respective probabilistic state spaces (symbol $\sim$), whose degrees of belief are provided by the conditional probability distributions $p(\boldsymbol{q}_k \mid \boldsymbol{q}_{k-1}, \boldsymbol{\theta}, \boldsymbol{F})$ and $p(\boldsymbol{y}_k \mid \boldsymbol{q}_k)$, respectively. We assume that (i) the physical model is described by a Markov chain; and (ii) observations are conditionally independent in time, which means that the probability of an observation depends only on the current state. The objective of data assimilation is to find the joint probability distribution $p(\boldsymbol{q}_{0:N}, \boldsymbol{y}_{1:N}, \boldsymbol{\theta}, \boldsymbol{F})$, which provides a complete statistical description because all the probability distributions of interest ensue from it. (The symbol : signifies that all states are considered, e.g., $\boldsymbol{q}_{0:N}$ signifies that the state $\boldsymbol{q}$ is considered from timestep 0 to N inclusive.) First, in *state estimation* the objective is to compute $p(\boldsymbol{q}_{0:N} \mid \boldsymbol{y}_{1:N}, \boldsymbol{\theta}, \boldsymbol{F})$, which provides the belief in a series of states given a physical model and parameters. Second, in *parameter estimation* the objective is to compute $p(\boldsymbol{\theta} \mid \boldsymbol{y}_{1:N}, \boldsymbol{F})$, which provides the belief in a set of parameters given a physical model. Parameter estimation can be combined with state estimation, where the parameters are concatenated in the state vector such that they are subject to the same probabilistic state space (Eq. (12)) [43]. Third, in *model comparison* the objective is to compute $p(\boldsymbol{F} \mid \boldsymbol{y}_{1:N})$, which provides the model that is more likely to be predictive as compared to other models. Practically, the joint probability distribution is rarely computed because the probabilistic state space, which spans multiple timesteps, is high dimensional [2]. Therefore, state estimation computes the conditional probability distribution at a single timestep. Conditional probability distributions that are relevant to state estimation are (i) filtering, (ii) smoothing and (iii) prediction. Filtering estimates our belief in the current state given observations in the past and present, i.e., $p(\boldsymbol{q}_k \mid \boldsymbol{y}_{1:k}, \boldsymbol{\theta}, \boldsymbol{F})$. Smoothing estimates our belief in the current state given observations in the past, future and present, i.e., $p(\boldsymbol{q}_k \mid \boldsymbol{y}_{1:N}, \boldsymbol{\theta}, \boldsymbol{F})$. Prediction estimates our belief in the future state given the observations in the past and present, i.e., $p(\boldsymbol{q}_{N+1} \mid \boldsymbol{y}_{1:N}, \boldsymbol{\theta}, \boldsymbol{F})$. In section 5.1, we will perform state estimation without smoothing through an ensemble Kalman filter. For smoothing, parameter estimation and model performance in premixed flames, the reader may refer to [42, 43].

3.1 Bayesian filter and ensemble Kalman filter

To introduce the ensemble Kalman filter with a Bayesian approach, we first explain the Bayesian filter. First, the state is predicted by the Chapman-Kolmogorov equation (prediction step)

$$p(\boldsymbol{q}_k \mid \boldsymbol{y}_{1:k-1}, \boldsymbol{\theta}, \boldsymbol{F}) = \int p(\boldsymbol{q}_k \mid \boldsymbol{q}_{k-1}, \boldsymbol{\theta}, \boldsymbol{F}) p(\boldsymbol{q}_{k-1} \mid \boldsymbol{y}_{1:k-1}, \boldsymbol{\theta}, \boldsymbol{F}) \, \mathrm{d}\boldsymbol{q}_{k-1}. \tag{14}$$

Typically, the Chapman-Kolmogorov equation, which involves a high dimensional integral, is solved by a Monte Carlo simulation. Second, the state is updated by the Bayes' rule (update step)

$$p(\boldsymbol{q}_k \mid \boldsymbol{y}_{1:k}, \boldsymbol{\theta}, \boldsymbol{F}) = \frac{p(\boldsymbol{y}_k \mid \boldsymbol{q}_k) p(\boldsymbol{q}_k \mid \boldsymbol{y}_{1:k-1}, \boldsymbol{\theta}, \boldsymbol{F})}{p(\boldsymbol{y}_k \mid \boldsymbol{y}_{1:k-1}, \boldsymbol{\theta}, \boldsymbol{F})}, \tag{15}$$

where the left-hand side is the posterior, the first term in the numerator of the right-hand side is the likelihood and the second term is the prior. The Bayesian filter is sequential in nature, which reduces the complexity of data assimilation and enables on-the-fly statistical learning. In the Kalman filter, the prior and the likelihood in the update step of the Bayesian filter are assumed to be normal, i.e., $p(\boldsymbol{q}_k \mid \boldsymbol{y}_{1:k-1}, \boldsymbol{\theta}, \boldsymbol{F}) = \mathcal{N}\left(\boldsymbol{q}_k \mid \boldsymbol{\psi}^f, \boldsymbol{C}^f_{\psi\psi}\right)$ and $p(\boldsymbol{y}_k \mid \boldsymbol{q}_k) = \mathcal{N}(\boldsymbol{y}_k \mid \boldsymbol{M}\boldsymbol{q}_k, \boldsymbol{C}_{\epsilon\epsilon})$, where $\mathcal{N}$ is a normal distribution with mean in the first argument and covariance matrix in the second argument. The measurement operator, $\boldsymbol{M}$, is assumed linear in this chapter. The mean of the prior is denoted by $\boldsymbol{\psi}^f$, the covariance matrix by $\boldsymbol{C}^f_{\psi\psi}$, and the covariance matrix of the likelihood, also known as the observation error, by $\boldsymbol{C}_{\epsilon\epsilon}$. The Kalman filter [27] finds the filtered distribution as follows

$$p(\boldsymbol{q}_k \mid \boldsymbol{y}_{1:k}, \boldsymbol{\theta}, \boldsymbol{F}) = \mathcal{N}\left(\boldsymbol{q}_k \mid \boldsymbol{\psi}^a, \boldsymbol{C}^a_{\psi\psi}\right), \tag{16}$$

$$\boldsymbol{\psi}^a = \boldsymbol{\psi}^f + \underbrace{\left(\boldsymbol{M}\boldsymbol{C}^f_{\psi\psi}\right)^T \left[\boldsymbol{C}_{\epsilon\epsilon} + \boldsymbol{M}\boldsymbol{C}^f_{\psi\psi}\boldsymbol{M}^T\right]^{-1}}_{\text{Kalman gain}} \underbrace{\left(\boldsymbol{y} - \boldsymbol{M}\boldsymbol{\psi}^f\right)}_{\text{Innovation}}, \tag{17}$$

$$\boldsymbol{C}^a_{\psi\psi} = \boldsymbol{C}^f_{\psi\psi} - \left(\boldsymbol{M}\boldsymbol{C}^f_{\psi\psi}\right)^T \left[\boldsymbol{C}_{\epsilon\epsilon} + \boldsymbol{M}\boldsymbol{C}^f_{\psi\psi}\boldsymbol{M}^T\right]^{-1} \left(\boldsymbol{M}\boldsymbol{C}^f_{\psi\psi}\right), \tag{18}$$

where the superscript f denotes *forecast* (everything related to the prediction), and the superscript a denotes *analysis* (everything related to the update). If the physical model is highly nonlinear, such as turbulent flows, the prediction of the covariance matrix $\boldsymbol{C}^f_{\psi\psi}$ for the Kalman filter is computed by Monte Carlo sampling. This is called the ensemble Kalman filter [17]. Instead of a mean $\boldsymbol{\psi}$ and a covariance matrix $\boldsymbol{C}_{\psi\psi}$, a distribution is represented by a sample $\boldsymbol{\psi}^j$, $j = 1, 2, \ldots n$ where n is the number of samples. During the prediction step, the ensemble members $\boldsymbol{\psi}^j$ evolve in time independently. Before the update step, the statistics are estimated from the sample as follows

$$\overline{\boldsymbol{\psi}} \approx \frac{1}{n}\sum_{j=1}^{n} \boldsymbol{\psi}^j \quad , \quad \boldsymbol{C}_{\psi\psi} \approx \frac{1}{n-1}\sum_{i=1}^{n} (\boldsymbol{\psi}^i - \overline{\boldsymbol{\psi}}) \otimes (\boldsymbol{\psi}^i - \overline{\boldsymbol{\psi}}), \tag{19}$$

where $\otimes$ is the dyadic product. The sample covariance matrix $\boldsymbol{C}_{\psi\psi}$ involves division by $n-1$ instead of n to avoid a sample bias. There exist several implementations of the ensemble Kalman filter, which differ in the update step. In the most straightforward implementation of the ensemble Kalman filter [17], each ensemble member is individually updated (Eq. (17)). In so doing, the observations must be randomly perturbed to guarantee a statistically consistent analysis scheme [6]. This is the approach used in this chapter. Alternatively, to avoid the introduction of randomly generated numbers in the observations, the square-root filter can be used [40, 43], where the mean and the deviations of the ensemble members are updated. While no spurious

errors due to the random perturbations of the observations are introduced, the square root filter requires a singular value decomposition.

3.1.1 Numerical implementation of the ensemble Kalman filter

The Kalman gain $\boldsymbol{K} \equiv \boldsymbol{C}^f_{\psi\psi}\boldsymbol{M}^T\left[\boldsymbol{C}_{\epsilon\epsilon} + \boldsymbol{M}\boldsymbol{C}^f_{\psi\psi}\boldsymbol{M}^T\right]^{-1}$ is not explicitly computed because it is more efficient to perform a number of matrix-vector computations from right to left. From Eq. (17), the i-th sample of the analysis is conveniently expressed as

$$\boldsymbol{\psi}^{a,i} = \boldsymbol{\psi}^{f,i} + \underbrace{\frac{1}{n-1}\sum_{j=1}^{n}\left(\boldsymbol{\psi}^{f,j} - \overline{\boldsymbol{\psi}^f}\right)\left[\boldsymbol{M}\left(\boldsymbol{\psi}^{f,j} - \overline{\boldsymbol{\psi}^f}\right)\right]^T}_{\boldsymbol{C}_{\psi\psi}\boldsymbol{M}^T}\boldsymbol{b}^i, \tag{20}$$

where $\boldsymbol{K}\boldsymbol{b}^i = \boldsymbol{y}^i - \boldsymbol{M}\boldsymbol{\psi}^{f,i}$. The parallel algorithm is summarized in the following gray box using the indices i and j as in(20).

1. Compute $\boldsymbol{y}^i - \boldsymbol{M}\boldsymbol{\psi}^{f,i}$ on each CPU i;
2. Compute $\overline{\boldsymbol{\psi}^f}$ (`MPI_Allreduce` to make it available on all CPUs);
3. Compute $\boldsymbol{\psi}^{f,j} - \overline{\boldsymbol{\psi}^f}$ on each CPU j;
4. Compute $\boldsymbol{M}\boldsymbol{C}_{\psi\psi}\boldsymbol{M}^T$ with $O(mn^2)$ operations as

$$\boldsymbol{M}\boldsymbol{C}_{\psi\psi}\boldsymbol{M}^T = \frac{1}{n-1}\sum_{j=1}^{n}\left[\boldsymbol{M}\left(\boldsymbol{\psi}^{f,j} - \bar{\boldsymbol{\psi}}\right)\right] \otimes \left[\boldsymbol{M}\left(\boldsymbol{\psi}^{f,j} - \bar{\boldsymbol{\psi}}\right)\right]; \tag{21}$$

5. Compute $\boldsymbol{C}_{\epsilon\epsilon} + \boldsymbol{M}\boldsymbol{C}^f_{\psi\psi}\boldsymbol{M}^T$;
6. Solve $\left(\boldsymbol{C}_{\epsilon\epsilon} + \boldsymbol{M}\boldsymbol{C}^f_{\psi\psi}\boldsymbol{M}^T\right)\boldsymbol{b}^i = \boldsymbol{y}^i - \boldsymbol{M}\boldsymbol{\psi}^{f,i}$ for $\boldsymbol{b}_i$ on each CPU i (e.g., with `LAPACK`), and collect all $\boldsymbol{b}^i$ on all CPUs (e.g., `MPI_Allgatherv`);
7. Compute the scalars $\left[\boldsymbol{M}\left(\boldsymbol{\psi}^{f,j} - \overline{\boldsymbol{\psi}^f}\right)\right]^T\boldsymbol{b}^i$ on each CPU j;
8. Compute $\boldsymbol{C}^f_{\psi\psi}\boldsymbol{M}^T\boldsymbol{b}_i$ and evaluate Eq. (20) on each CPU i (`MPI_Reduce`).

The ensemble covariance matrix $\boldsymbol{C}^f_{\psi\psi}$ of the model prediction has rank $n-1$, and so does the m-by-m matrix $\boldsymbol{M}\boldsymbol{C}^f_{\psi\psi}\boldsymbol{M}^T$. Depending on the covariance matrix $\boldsymbol{C}_{\epsilon\epsilon}$ of the measurement, the m-by-m matrix $\boldsymbol{C}_{\epsilon\epsilon} + \boldsymbol{M}\boldsymbol{C}^f_{\psi\psi}\boldsymbol{M}^T$ may be singular. Therefore, if $n \leq m$, the matrix $\boldsymbol{M}\boldsymbol{C}^f_{\psi\psi}\boldsymbol{M}^T$ is rank deficient. In the absence of measurement errors, solving the linear system in item 6 is a minimum-norm least-squares problem. An alternative approach is to use the square root filter (Section 3.1). Note that a finite ensemble size can cause the covariance to be underestimated, which can lead to covariance collapse [39]. There are a few tricks to avoid this, such as a simple

covariance inflation [1, 41]

$$\boldsymbol{\psi}^{a,i} = \overline{\boldsymbol{\psi}^{a}} + \beta(\boldsymbol{\psi}^{a,i} - \overline{\boldsymbol{\psi}^{a}}) + \boldsymbol{\alpha}, \tag{22}$$

where β is the multiplicative covariance inflation, which could be a scalar or a matrix, and $\boldsymbol{\alpha}$ is the additive covariance inflation, which is a vector.

4 Direct numerical simulation of MILD combustion

In this chapter, the analysis methods described in sections 2 and 3 are applied to Direct Numerical Simulation (DNS) of Moderate or Intense Low-oxygen Dilution (MILD) combustion. The DNS data considered for this analysis is generated following the methodology presented in [13]. The configuration is a non-premixed methane/diluted air MILD combustion with internal EGR at atmospheric pressure. The DNS domain is a cube of 1 cm^3 with inflow/non-reflecting Navier-Stokes Characteristic Boundary Conditions (NSCBC) [36] outflow boundary conditions in the x-direction and periodic boundary conditions in the y and z directions. As to the generation of the initial conditions, in a first preprocessing stage, initial fields of turbulence, mixture fraction, Z, reaction progress variable c, and species mass fractions, Y_α, are generated. To do so, first, laminar premixed flames under MILD combustion conditions are computed for various values of Z and the scalar mass fractions are tabulated as a function of Z and c. Subsequently, initial 3D reaction progress variable and mixture fraction fields are generated with prescribed means, $\langle Z \rangle$ and $\langle c \rangle$, and lengthscales, ℓ_Z and ℓ_c using the method of [16]. Z is defined using Bilger's definition [3] and the progress variable is based on the fuel mass fraction. The scalar mass fractions from the laminar flames calculations are then mapped onto these 3D fields. Additionally, an initial decaying homogeneous isotropic turbulence field is generated with the required turbulence characteristics. This turbulence field is then combined with the scalar fields previously generated, which interact in a non-reacting simulation for about one large eddy turnover time to ensure that the velocity-scalar correlations have sufficiently evolved. The fields obtained are then used as the initial and inflowing conditions for the second stage, which is the actual reacting DNS of MILD combustion. Further details on this methodology can be found in [13].

In this chapter, DNS similar to the AZ1 case of [13] with a 512^3 mesh is performed. The initial characteristics of this DNS are summarized in Table 1. Additionally, the oxidizer considered is composed of 3.5% of O_2, 13.4% of H_2O, 6.7% of CO_2 and 76.4% of N_2. The initial turbulence Reynolds numbers based on the integral length scale and Taylor microscale are respectively $\mathrm{Re}_t = 96$ and $\mathrm{Re}_\lambda = 34.73$. The chemical mechanism used here is an extended version of the Smooke methane/air mechanism as detailed in [13]. We removed OH^* chemistry to allow the timestep to be larger, i.e., $\Delta t = 10ns$. A study of the chemical markers, such as OH^*, can be found in [12].

Table 1 DNS initial conditions. Λ_0 is the integral lengthscale, η is the Kolmogorov lengthscale and u' is the initial root- mean square value of the velocity fluctuations.

Grid	Λ_0/ℓ_Z	$\langle X_{O_2} \rangle$	$X_{O_2}^{max}$	ℓ_Z/ℓ_c	$\langle Z \rangle$	Z_{st}	σ_Z	$\langle c \rangle$	σ_c	u' [m/s]	η [μs]
512^3	0.60	0.0270	0.035	1.30	0.008	0.010	0.0084	0.56	0.26	16.67	47.7

A typical heat release rate field is presented in Fig. 2. There exist multiple iso-surfaces of heat release rate that are not confined to thin reaction zones, where both ignition and deflagration combustion modes can be found [11].

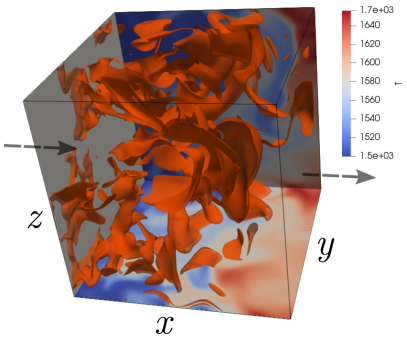

Fig. 2: Isosurface of heat release rate field in DNS of MILD combustion (threshold at $\dot{Q} = 1.75 \cdot 10^8$ $[W/m^3]$) with temperature field (in [K]) on the bottom and side surfaces.

In addition to the fine DNS with a 512^3 mesh, DNS on coarser grids of 96^3, 128^3 and 256^3 points are performed. These DNS are initialized using the solution of the fine DNS after it has reached a steady state. The DNS is run with the code SENGA2 [7] which solves the fully compressible reacting Navier-Stokes equations with a 10th order finite difference scheme for spatial discretization and a third order low-storage Runge-Kutta scheme for time integration on CSD3 (Cambridge, UK), a Tier-2 cluster.

5 Results

5.1 Predictability of DNS of MILD combustion

Following the procedure described in section 2, the predictability of the DNS of MILD combustion is assessed on coarse DNS grids with respectively, 96^3, 128^3 and 256^3 grid points. Each simulation is initialized from the last snapshot of a statistically converged DNS on the 512^3 grid. Subsequently, the inlet velocity of the

coarse simulations are perturbed, with $\epsilon = 10^{-3}$ and the separation trajectory of each simulation is presented in Fig. 3.

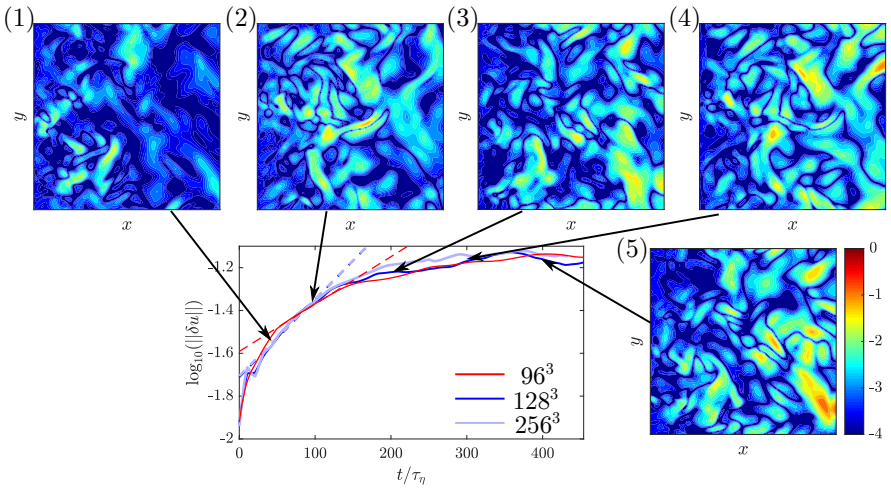

Fig. 3: Separation based on velocity as a function of time with meshes 96^3 (red), 128^3 (blue) and 256^3 (violet). The dashed lines indicate the slope of the linear region of the separation trajectories. Additional panels show the mid x-y plane of the norm of the separation trajectory, $\log_{10}(||\delta u||)$, for the mesh 128^3. In the linear region, this is the norm of the covariant Lyapunov velocity vector.

The values of the Lyapunov exponent, extracted by linear regression, highlighted using dashed lines in Fig. 3, are summarized in Table 2. It is seen that the Lyapunov exponent increases between the 96^3 and 128^3 and saturates for 256^3. This indicates that most of the chaotic dynamics is captured by the 128^3 grid. Furthermore, the separation frames highlight that the separation occurs in the upstream region of the domain where the decaying isotropic turbulence is being injected into the domain (see panels (1) and (2) in Fig. 3). In that region, the separation originates chiefly because of how the perturbed and unperturbed velocity fields are evolving into different turbulence fields, upstream of the main heat release regions.

Table 2 Lyapunov exponents and predictability of the MILD combustion configuration.

	96^3	128^3	256^3
$\lambda\tau_\eta$	0.00509	0.00835	0.00826
$1/(\lambda\tau_\eta)$	195.46	119.76	121.06
$t_p = 1/\lambda$ [μs]	562.2	342.7	346.4

In addition to the first highlighted linear region, there appears a second seemingly linear region for $t/\tau_\eta = 200$ to 300. This suggests that another phenomenon is responsible for the separation of the simulations at a later time. Indeed, large separation downstream of reaction zones appear and contribute to the increase in separation between the simulations (see panels (3) and (4) in Fig. 3). This separation is due to the diverging heat release rate fields, which yields different velocity fields downstream of the reaction zones. We conjecture that the change in slope is linked to the change in timescale between the regions upstream and downstream of the reaction zones, i.e., the downstream region has a much smaller turbulence level due to the heat release. Finally, it should be noted that the particular DNS cases have a quite limited Reynolds number and have high temperature with large viscosity. As a result, the Lyapunov exponents of MILD combustion are smaller than those of the forced-homogeneous isotropic turbulence of [32]. Combustion makes a turbulent flow more predictable from a dynamical systems point of view.

5.2 State estimation of DNS of MILD combustion

The ensemble Kalman filter described in section 3 is applied here to improve the prediction of the heat release rate evolution in the DNS of MILD combustion. In the present problem, the measurements are taken from the finely resolved DNS (on the 512^3 mesh) and the forecasts are obtained by running an ensemble of 10 coarse DNS, each with a mesh of 128^3 nodes. The initial velocity field for each coarse DNS is perturbed by a factor $\epsilon||u||$ where ϵ is a random number following a Gaussian distribution centred around 10^{-3} with standard deviation of 10^{-4}. The observations from the fine DNS, which mimic observations from an experimental rig, are located in a cube of length 3mm centred around the point $(3.149, 3.149, 3.149)$ [mm] as illustrated in Fig. 4. It was observed from the fine DNS that this location corresponds to a region where both ignition and flame propagation occur, which are difficult to predict accurately in space and time. Therefore, this region is a spot-on location where to apply data assimilation to appreciate its performance. In the observation box, sampling locations are uniformly distributed with 21 samples in each direction for a total of 9261 sampling locations. At each of these locations, the values of velocity (u, v and w), Y_{OH} and $Y_{\mathrm{CH_2O}}$ are collected from the fine DNS to mimic experimental measurements from Particle Image Velocimetry (PIV) or Planar Laser-Induced Fluorescence (PLIF). The state vector, $\boldsymbol{\psi}$, is taken to be the same as the experimental measurements, hence, the observation matrix $\boldsymbol{M}$ is the identity matrix. Furthermore, the observation error is taken to be the standard deviation of the observed quantity in a smaller cube of length $78\mu m$, which corresponds to 1/40 of the entire observation box centred around each measurement location from the fine DNS. This corresponds to passing from the fine grid of 512^3 nodes to 128^3 nodes on the coarse DNS. Data assimilation is performed every $40\mu s$, which corresponds to approximately one tenth of the average ignition delay time for the mixture under study. The evolution of the logarithm of the Root Mean Squared

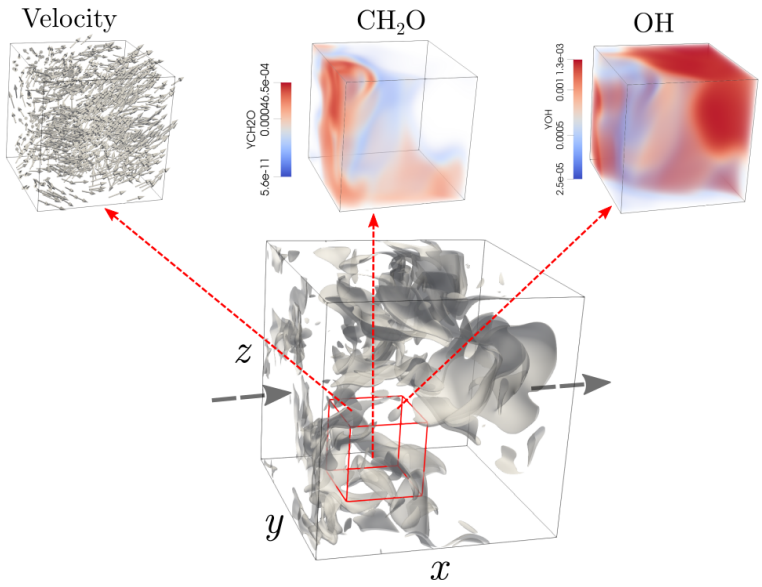

Fig. 4: Observation box (in red), where the measured quantities (velocity field, CH_20 and OH) are taken.

(RMS) error (RMSE), computed as the trace of the ensemble covariance matrix, RMSE = $\mathrm{tr}(\boldsymbol{C}^f_{\boldsymbol{\psi}\boldsymbol{\psi}})$ where $\boldsymbol{\psi}$ is just composed of the measured states is shown in Fig. 5a. At the beginning, the RMS error is small because nearly identical initial conditions are used for all cases. Because of the chaotic nature of the turbulence flow, the RMS subsequently grows. At each data-assimilation event, the uncertainty is markedly decreased by approximately half a decade. Another metric to assess how more predictive the filtered solution is with respect to the unfiltered solution is the evolution of the normalized error of the heat release rate (Fig. 5b)

$$\widetilde{\Delta\dot{Q}} = \frac{\sqrt{\int_V (\dot{Q}_m - \dot{Q}_c)^2 dV}}{\int_V \dot{Q}_m dV} \tag{23}$$

which is integrated in the observation box, V, where $\dot{Q}_m$ is the heat release rate computed on the fine DNS and $\dot{Q}_c$ is either the heat release rate from the coarse DNS (red line in Fig. 5b) or the one from the mean evolution obtained from the Kalman Filter procedure (blue line in Fig. 5b). It can be observed that the Ensemble Kalman Filter procedure allows for an improvement on the prediction of the evolution of the heat release rate with an overall lower error. In addition to these global statistics, Fig. 6 illustrates the evolution of the heat release rate in the observation box during the time period shown in Fig. 5 for the fine DNS with a mesh of 512^3, the coarse DNS with a mesh of 128^3 and the mean field from the Ensemble Kalman filter method, denoted EnsKal DNS in the following. In frames (1) and (2), the morphology of the reaction

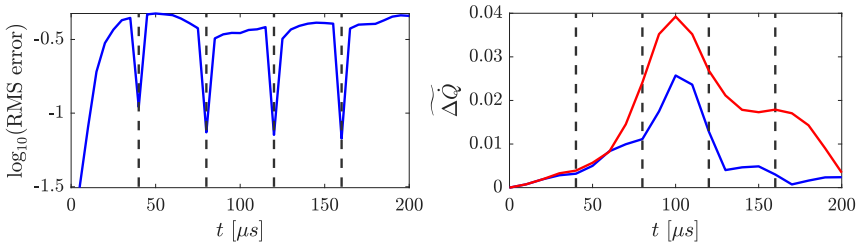

Fig. 5: Evolution of the (left) RMSE and (right) normalized error of $\dot{Q}$ from the coarse DNS (red) and the average evolution from the Ensemble Kalman Filter (blue). Dashed vertical lines indicate when the data from the fine DNS is assimilated.

zones are approximately the same for all simulations as they are evolving from the same initial field (or the slightly perturbed field in the case of the Ensemble Kalman filter). The coarse features of the reaction zones for the coarse and EnsKal DNS come from the under-resolved DNS, which cannot capture all the detailed morphological features of the fine DNS. In frame (3), which is after the first data-assimilation event, a specific ignition kernel is highlighted. While both the coarse and EnsKal DNS show that they capture that feature, its evolution in time (frame (4)) is fuller and more quantitatively accurate in the EnsKal DNS. This indicates that the EnsKal DNS has assimilated the correct consumption of species, in particular of CH_2O, which acts as a precursor, to predict the heat release morphology. Additionally, in frame (5), one can observe another ignition kernel, highlighted in the blue box, whose shape has been better captured by EnsKal DNS. From frame (5) to (6), there are major reaction zones interaction, which roughly corresponds to the peak in error at $t = 100\mu s$ in Fig. 5b. From frame (5) to (7), one can observe the evolution of the previous reaction zone, which has merged with neighbouring reaction zones to form a deflagrative structure. While the merging is captured by all the simulations, the morphology of the EnsKal DNS more accurately represents the morphology of the fine DNS. This is thanks to the successful assimilation of the velocity field, which is an essential physical quantity to assimilate for the propagation of the various interacting reaction zones. In conclusion, the turbulent MILD combustion case presented highlights how data assimilation enables space-and-time accurate prediction of both macroscopic quantities (volumetric heat release rate, Fig. 5b) and local quantities (heat release morphology, Fig. 6).

6 Conclusions and future directions

The butterfly effect limits the time-accurate prediction of turbulent flows, which are chaotic flows. Tools from chaos theory and statistical learning are, thus, called upon. The inverse of the dominant Lyapunov exponent provides an estimate of the predictability of the flow, which is a characteristic time horizon within which the

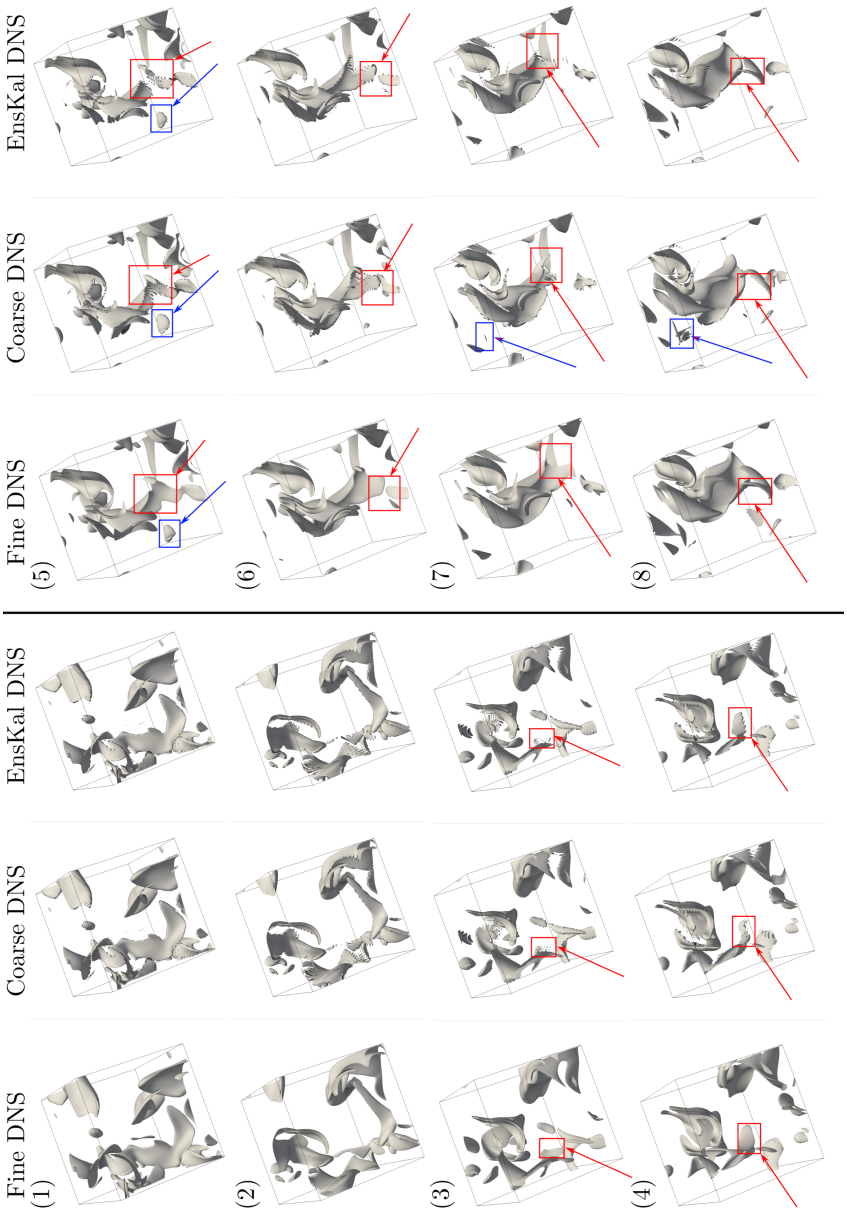

Fig. 6: Evolution of the isosurface of $\dot{Q} = 1.75 \cdot 10^8$ $[W/m^3]$ in the observation box during the simulation (left: fine DNS, middle: coarse DNS, right: average of the ensemble). Red and blue boxes highlight some of the key features. Panels 1 to 8 are respectively for $t = 0,\ 35,\ 60,\ 80,\ 105,\ 120,\ 140,\ 155\mu s$ in Fig. 5b.

butterfly effect makes two nearby trajectories diverge. The ensemble Kalman filter enables statistical learning of the state given predictions from a physical model and observations from a more refined simulation or laboratory experiments. We use Lyapunov theory and the ensemble Kalman filter on a turbulent reacting problem relevant to Moderate or Intense Low-oxygen Dilution (MILD) combustion. In MILD combustion, it is paramount to accurately capture ignition kernels and their evolutions towards deflagration because this interplay stabilizes the combustion process. The occurrence and dynamics of ignition kernels is seemingly random (albeit deterministic) due to this turbulent mixture containing high temperature spots and recirculating radicals. So assessing the predictability of our simulations helps to determine whether they can reliably capture such transient events, for example in terms of the mesh size requirements. By assimilating data from a refined simulation, the ensemble Kalman filter greatly improves the space-and-time accurate prediction in an under-resolved simulation by detecting the occurrence of ignition kernels, the stabilization of deflagrative modes and intricate changes in the flow morphology. The physics-informed data-driven methods presented open up new possibilities for the space-and-time accurate prediction of rare and transient events in turbulent flows by combining an under-resolved simulation, or a reduced order model, with data from experiments. As an example, this can be exploited to learn and calibrate subgrid-scale models for large-eddy simulation.

Acknowledgements The authors acknowledge the support of the Technical University of Munich - Institute for Advanced Study, funded by the German Excellence Initiative and the European Union Seventh Framework Programme under grant agreement no. 291763. L. Magri also acknowledges the Royal Academy of Engineering Research Fellowships Scheme. This work was performed using resources provided by the Cambridge Service for Data Driven Discovery (CSD3) operated by the University of Cambridge Research Computing Service (www.csd3.cam.ac.uk), provided by Dell EMC and Intel using Tier-2 funding from the Engineering and Physical Sciences Research Council (capital grant EP/P020259/1), and DiRAC funding from the Science and Technology Facilities Council (www.dirac.ac.uk). The authors acknowledge Prof. Cant for providing the code SENGA2. Francisco Huhn and Hans Yu are gratefully acknowledged for their invaluable input on Lyapunov analysis (section 2) and data assimilation (section 3), respectively.

References

[1] J. L. Anderson and S. L. Anderson. A Monte Carlo Implementation of the Nonlinear Filtering Problem to Produce Ensemble Assimilations and Forecasts. *Monthly Weather Review*, 127(12):2741–2758, 2002.

[2] R. Bellman. *Dynamic programming*. Dover Publications, 2003.

[3] R. W. Bilger, S. H. Starner, and R. J. Kee. On reduced mechanisms for methane-air combustion in nonpremixed flames. *Combust. Flame*, 80:135–149, 1990.

[4] P. J. Blonigan, P. Fernandez, S. M. Murman, Q. Wang, G. Rigas, and L. Magri. Towards a chaotic adjoint for LES. In *Center for Turbulence Research, Summer Program*, 2016.

[5] G. Boffetta, M. Cencini, M. Falcioni, and A. Vulpiani. Predictability: a way to characterize complexity. *Physics Reports*, 356:367–474, 2002.
[6] G. Burgers, P. J. van Leeuwen, and G. Evensen. Analysis scheme in the ensemble Kalman filter. *Monthly Weather Review*, 126(6):1719–1724, June 1998.
[7] R. S. Cant. SENGA2 User Guide (CUED–THERMO–2012/04, 2nd edition). Technical report, University of Cambridge, 2013.
[8] A. Cavaliere and M. de Joannon. Mild combustion. *Prog. Energy Combust. Sci.*, 30:329–366, 2004.
[9] A. F. C. da Silva and T. Colonius. Ensemble-Based State Estimator for Aerodynamic Flows. *AIAA Journal*, 56(7):2568–2578, 2018.
[10] D. Darakananda, A. F. D. C. Da Silva, T. Colonius, and J. D. Eldredge. Data-assimilated low-order vortex modeling of separated flows. *Physical Review Fluids*, 3(12):1–24, 2018.
[11] N. A. K. Doan and N. Swaminathan. Autoignition and flame propagation in non-premixed MILD combustion. *Combust. Flame*, 201:234–243, 2019.
[12] N. A. K. Doan and N. Swaminathan. Analysis of Markers for Combustion Mode and Heat Release in MILD Combustion Using DNS Data. *Combust. Sci. Technol.*, 191(5-6):1059–1078, 2019.
[13] N. A. K. Doan, N. Swaminathan, and Y. Minamoto. DNS of MILD combustion with mixture fraction variations. *Combust. Flame*, 189:173–189, 2018.
[14] A. Doucet, N. Freitas, and N. Gordon, editors. *Sequential Monte Carlo Methods in Practice*. Springer New York, 2001.
[15] J. P. Eckmann and D. Ruelle. Ergodic theory of chaos and strange attractors. *Reviews of Modern Physics*, 57:617–656, 1985.
[16] V. Eswaran and S. B. Pope. Direct numerical simulations of the turbulent mixing of a passive scalar. *Phys. Fluids*, 31(3):506–520, 1988.
[17] G. Evensen. Sequential data assimilation with a nonlinear quasi-geostrophic model using Monte Carlo methods to forecast error statistics. *Journal of Geophysical Research*, 99(C5):10143, 1994.
[18] G. Evensen. *Data Assimilation - The Ensemble Kalman Filter*. Springer, 2009.
[19] J. D. Farmer, E. Ott, and J. A. Yorke. The dimension of chaotic attractors. *Physica D*, 7(1-3):153–180, 1983.
[20] P. Fernandez and Q. Wang. Lyapunov spectrum of the separated flow around the NACA 0012 airfoil and its dependence on numerical discretization. *Journal of Computational Physics*, 350:453–469, 2017.
[21] F. Ginelli, H. Chaté, R. Livi, and A. Politi. Covariant lyapunov vectors. *Journal of Physics A: Mathematical and Theoretical*, 46(25):254005, 2013.
[22] I. Goldhirsch, P.-L. Sulem, and S. A. Orszag. Stability and Lyapunov stability of dynamical systems: A differential approach and a numerical method. *Physica D: Nonlinear Phenomena*, 27(3):311–337, 1987.
[23] M. Hassanaly and V. Raman. Ensemble-LES analysis of perturbation response of turbulent partially-premixed flames. *Proceedings of the Combustion Institute*, 37(2):2249–2257, 2019.
[24] R. C. Hilborn. *Chaos and Nonlinear Dynamics*. Oxford University Press, 1994.

[25] F. Huhn and L. Magri. Stability , sensitivity and optimisation of chaotic acoustic oscillations. *Journal of Fluid Mechanics, to appear*, 2019.
[26] F. Huhn and L. Magri. Stability , sensitivity and optimisation of a chaotically perturbed acoustic system. *Nonlinear dynamics, under review*, 2019.
[27] R. E. Kalman. A New Approach to Linear Filtering and Prediction Problems. *Journal of Basic Engineering*, 82(1):35, 1960.
[28] J. W. Labahn, H. Wu, B. Coriton, J. H. Frank, and M. Ihme. Data assimilation using high-speed measurements and les to examine local extinction events in turbulent flames. *Proceedings of the Combustion Institute*, 37(2):2259–2266, 2019.
[29] E. N. Lorenz. Deterministic nonperiodic flow. *Journal of the Atmospheric Sciences*, 20(2):130–141, 1963.
[30] Y. Minamoto, N. Swaminathan, R. S. Cant, and T. Leung. Morphological and statistical features of reaction zones in MILD and premixed combustion. *Combust. Flame*, 161(11):2801–2814, nov 2014.
[31] P. Mohan, N. Fitzsimmons, and R. D. Moser. Scaling of Lyapunov Exponents in Homogeneous Isotropic Turbulence. *Physical Review Fluids*, 2:114606, 2017.
[32] G. Nastac, J. Labahn, L. Magri, and M. Ihme. Lyapunov exponent as a metric for assessing the dynamic content and predictability of large-eddy simulations. *Physical Review Fluids*, 2(9):094606, 2017.
[33] A. Ni and Q. Wang. Sensitivity analysis on chaotic dynamical systems by Non-Intrusive Least Squares Shadowing (NILSS). *Journal of Computational Physics*, 347:56–77, 2017.
[34] V. I. Oseledets. A multiplicative ergodic theorem: Lyapunov characteristic numbers for dynamical systems. *Trans. Moscow Math. Soc.*, 19:197–231, 1968.
[35] I. B. Özdemir and N. Peters. Characteristics of the reaction zone in a combustor operating at mild combustion. *Exp. Fluids*, 30:683–695, 2001.
[36] T. Poinsot. Boundary conditions for direct simulations of compressible viscous flows. *Journal of Computational Physics*, 101:104–129, apr 1992.
[37] S. B. Pope. Ten questions concerning the large-eddy simulation of turbulent flows. *New Journal of Physics*, 6, 2004.
[38] D. Ruelle. Ergodic Theory of Differentiable Dynamical Systems. *Publications mathematiques de l'IHES*, 50(1):27–58, 1979.
[39] P. J. van Leeuwen. Comment on "Data Assimilation Using an Ensemble Kalman Filter Technique". *Monthly Weather Review*, 127(6):1374–1377, 2002.
[40] J. S. Whitaker and T. M. Hamill. Ensemble Data Assimilation without Perturbed Observations. *Monthly Weather Review*, 130(7):1913–1924, July 2002.
[41] J. S. Whitaker and T. M. Hamill. Evaluating Methods to Account for System Errors in Ensemble Data Assimilation. *Monthly Weather Review*, 140(9): 3078–3089, 2012.
[42] H. Yu, T. Jaravel, M. Juniper, M. Ihme, and L. Magri. Data assimilation and optimal calibration in nonlinear models of flame dynamics. *ASME Turbo Expo GT2019-92052*, 2019.

[43] H. Yu, M. P. Juniper, and L. Magri. Combined State and Parameter Estimation in Level-Set Methods. *Journal of Computational Physics, under review*, pages 1–51, 2019.